Multifunctional Ultra-Wide-Angle Spatial Optical Analog Computing in the Terahertz Regime

Yongliang Liu, Bo Yu, Lesiqi Yin, Wenwei Liu, Qi Liu, Yifei Xu, Minghui Deng, Zhancheng Li, Cheng Gong*, Hua Cheng* and Shuqi Chen**

(Yongliang Liu, Bo Yu and Lesiqi Yin contributed equally to this work)

Y. Liu, B. Yu, W. Liu, Q. Liu, Y. Xu, Z. Li, H. Cheng, S. Chen

The Key Laboratory of Weak Light Nonlinear Photonics, Ministry of Education, School of Physics and TEDA Institute of Applied Physics, Nankai University, Tianjin 300071, China

E-mail: wliu@nankai.edu.cn; hcheng@nankai.edu.cn; schen@nankai.edu.cn

L. Yin, M. Deng and C. Gong

Institute of Modern Optics, Nankai University, Tianjin Key Laboratory of Micro-scale Optical Information Science and Technology, Tianjin, 300350, China

E-mail: gongcheng@nankai.edu.cn

C. Gong

Academy for Advanced Interdisciplinary Studies, Nankai University, Tianjin, 300350, China

S. Chen

School of Materials Science and Engineering, Smart Sensing Interdisciplinary Science Center, Nankai University, Tianjin 300350, China

S. Chen

The Collaborative Innovation Center of Extreme Optics, Shanxi University, Taiyuan 030006, China

Funding: This work was supported by the National Key Research and Development Program of China (2024YFA1409903 and 2021YFA1400601), the National Natural Science Foundation of China (12192253, 12274239, 12274237, 12474331, and U22A20258), and the Fundamental Research Funds for the Central Universities (63241331).

Keywords: Spatial differentiation, Metasurface, Terahertz, Edge detection, High resolution

Optical analog spatial differentiation, as the core mathematical operation in optical computing, can realize real-time edge detection in image processing and efficient feature extraction in data compression. Although analog spatial differential operations have been implemented in various optical systems, they still suffer from complex structural parameters dependency and a typically limited numerical aperture (NA) of smaller than 0.5. To date, achieving simultaneous first- and second-order spatial differentiation with NA higher than 0.5 remains an unresolved challenge, even considering recent advances in metasurface-based analog computing. Here, we propose a synergistic mechanism combining critical coupling and near-far-field multi-wave superposition to simultaneously achieve ultra-high-NA analog spatial first- and second-order differentiation. Operating in two orthogonal polarization modes, numerical simulations indicate that the maximum angle of incidence can reach 89.9°, corresponding to an NA approaching unity and yielding a spatial resolution limit of 1.27λ. Experimentally, the maximum incident angle achieved is 75°, corresponding to an NA of 0.966 and a spatial resolution limit of 1.3λ. We also propose the theoretical imaging resolution limit Δ(NA, λ) for edge detection. Our strategy significantly expands analog spatial computing to the non-paraxial region, which is pivotal in the upcoming high-speed communication, and can benefit future multifunctional terahertz imaging, computational analysis, medical diagnostics, and machine vision.

1. Introduction

The exponential growth of global data traffic has greatly boosted the development of communication and information processing networks with large capacity and high parallelism. Terahertz (THz) band (0.1–10 THz) technology, as a promising candidate for sixth-generation communication technologies, can potentially achieve terabit-per-second wireless links, bringing innovative solutions to information processing in the post-Moore's Law era.[1,2] Unlike visible light, which suffers from scattering losses, the THz band provides high resolution and remarkable penetration capability through obscurants like smoke and dust.[3] When compared with the microwave band, THz waves possess an intrinsic superiority in capacity and data speed, a direct benefit of their higher operating frequency.[4] Furthermore, under the action of electromagnetic resonances, THz waves can directly couple with molecular vibration and lattice resonance modes, making them suitable for safety detection and imaging in biomedical fields.[5] One of the most promising THz communication technologies utilizes concurrent optical analog computing to provide ultra-high throughput and low power consumption, surpassing traditional electronic systems.[6,7] For example, logic gates[8] and neural networks[9] have been demonstrated to realize efficient signal processing. To date, optical analog computing is reshaping the technological paradigms in fields such as computing, imaging, and communications. Although recent researches have endeavored to develop THz devices for information processing and computing such as beamformers,[10] arbitrary spatial projection,[11] and reconfigurable signal processors,[12,13] THz optical analog computing such as integration and differentiation, remains a largely unexplored field that still requires extensive investigation.

Spatial optical analog computing involves modulating the wavefronts of incident light in the spatial or momentum space,[14-16] thereby realizing various mathematical operations with 2-dimensional spatial parallelism. Spatial differentiation, as a cornerstone operator in optical analog computing, enables versatile functionalities such as edge-enhanced imaging[17,18] and phase singularity detection[19,20]. To date, spatial differentiation has been implemented through diverse strategies, including the Brewster effect,[21] guided resonances,[22,23] topological photonic bandgap,[24] bound states in the continuum [25,26] and the spin Hall effect.[27] However, owing to the difficulties in accurate manipulation of angular dispersion in both resonant and non-resonant electrodynamics,

current researches suffer from a typically limited numerical aperture (NA) of about 0.5, especially for multifunctional spatial analog computing.[28] Such a limitation significantly hinders non-paraxial applications such as full-angle communications, augmented reality and autonomous traffic. Although near-field-couplings metasurfaces might provide a solution,[29] it struggles to eliminate the polarization differences in optical responses for wide-angle incidences, mainly because different polarization states in a photonic system generally correspond to intrinsic distinct band modes or equivalent impedances, which in turn give rise to a series of phenomena such as various polarized dispersions and the Brewster effect.

Here, to address the limited NA challenge for different optical analog computing functions under various operating polarization states, we propose a scheme combining critical coupling and near-far-field multi-wave superposition to achieve the tailoring of momentum space with a metasurface in the terahertz regime. The metasurface can significantly manipulate the polarized angular dispersion, enabling second-order and first-order spatial differentiation operations with a large NA. The required transfer function is directly realized in the Fourier space to perform spatial filtering of an image by using the angular-dependent response of a meta-structure array. To the best of our knowledge, we also propose for the first time the resolution limit for edge imaging and differentiation. Our design is beneficial for achieving ultra-high spatial resolution in the THz regime with potential applications such as medical diagnostics, machine vision, and high-precision communication.

2. Results

To realize high-NA multifunctional analog spatial computing, we designed a metasurface composed of two connected U-shaped split rings (SRs) on a polyimide (PI) substrate with a ground metal layer. The unit cell of the metasurface is shown in Figure 1a, in which the thickness of the Au SRs, the PI substrate, and the ground Au film are 0.2 μm, 125 μm, and 0.2 μm, respectively. The periods in both the x and y directions are $P_x = P_y = 1400$ μm, and the permittivity and loss tangent of PI are considered as $\varepsilon_r = 3.5$ and $\delta = 0.0027$ in the THz region.[30] The conductivity of Au is 4.56×10^7 S/m.[31] The geometric parameters of the meta-structure are: a = 980 μm, b = 620 μm, c = 240 μm, d = 144 μm. For smaller incident angles, the metasurface performs as a polarized Fabry-Perot (FP)

resonator, which can realize tailorable polarization conversion for the required angular dispersion. When the incident angle approaches the grazing angle, another effect of critical coupling dominates accordingly, resulting in an extremely wide operating angle for the second-order differentiator, as shown in Figure 1b. Besides, destructive interference of the generated LSPs across distinct regions corresponds to the first-order differentiator. We will discuss the mechanism in detail in the following sections.

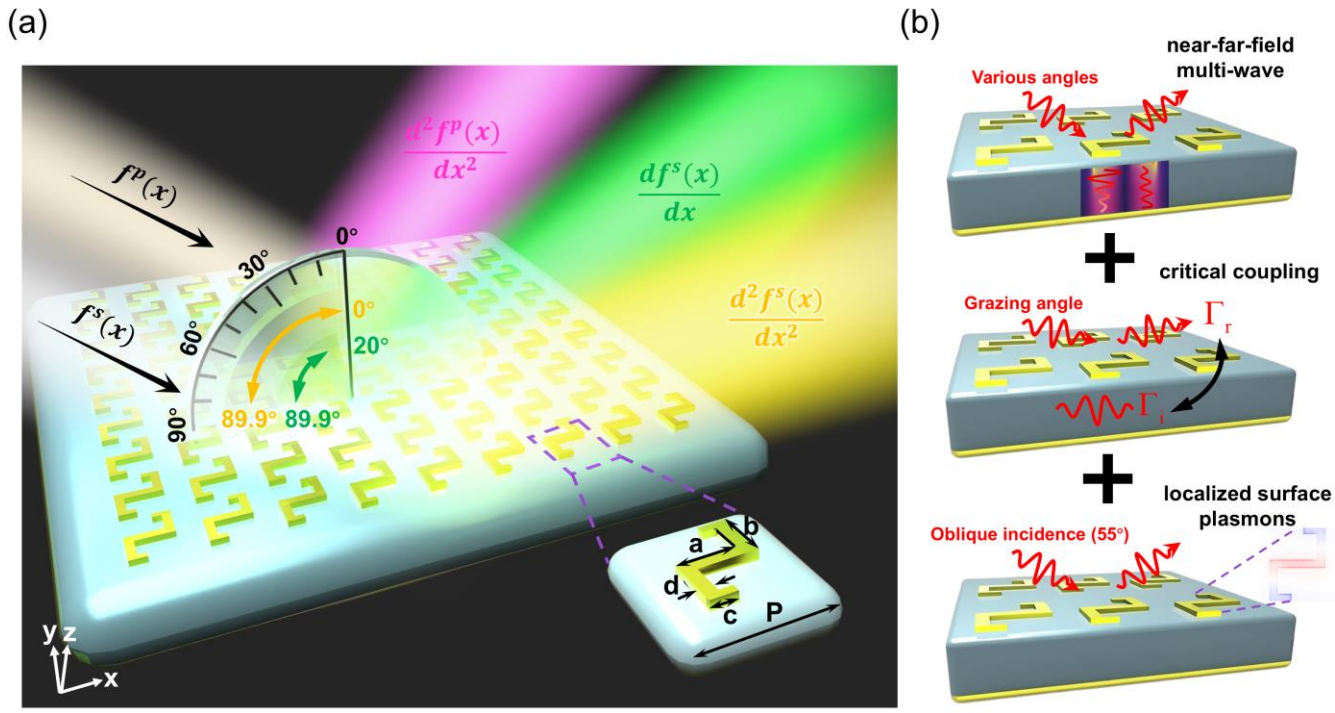

Figure 1. Schematic of the high-NA multifunctional analog differentiation operation. a) Numerical simulations show that, for *s*-polarized incidence, the differentiator performs the first- and second-order spatial differentiations, with angular bandwidths of 20°–89.9° and 0°–89.9°, respectively. For *p*-polarized incidence, the differentiator achieves second-order spatial differentiation, with an angular bandwidth of 0°–89.9°. The lower right corner is the unit cell of the designed differentiator. b) The synergistic mechanism of critical coupling, near-far-field multi-wave interference, and localized surface plasmons (LSPs) enables ultra-high-NA analog spatial first-/second-order differentiation.

According to the differential properties of the Fourier transform, the second-order spatial differentiation in real space is equivalent to quadratic filtering in the momentum space:[32]

$$H\left(k_x\right) = -\alpha k_x^{\,2}, \tag{1}$$

where H is the scattering function in momentum space, $k_x = k_0\sin\theta$ is the transverse momentum, k_0 is the wave number in free space, θ is the incident angle, and α is a constant. The maximum θ decides the operating NA and thus the maximum spatial resolution that can be processed by the metasurface. Note that the resolution limit is different from the one defined by the Rayleigh diffraction limit. As shown in Figure 2a, the metasurface can be modelled as a polarized FP resonator with polarization conversion. Without losing generality, when the distance between the microstructure array and the underlying metal is sufficiently large such as h = 800 μm, the reflective performance of the metasurface can be fully described by the classical multireflection model calculated by far-field S-parameters as reported in Refs. [33, 34]. The complex electric field amplitudes on different interfaces, i.e., E_{1x}^{-}, E_{2x}^{-} and E_{1y}^{-}, can be written as:

$$E_{1x}^{-} = E_{1x}^{+} r_{12}^{xx} + E_{1y}^{+} r_{12}^{xy} + E_{2x}^{-} t_{21}^{xx} e^{-i\beta h} + E_{2y}^{-} t_{21}^{xy} e^{-i\beta h}, \tag{2}$$

$$E_{2x}^{+} = E_{1x}^{+} t_{12}^{xx} e^{-i\beta h} + E_{2x}^{-} r_{21}^{xx} e^{-i2\beta h} + E_{2y}^{-} r_{21}^{xy} e^{-i2\beta h}, \tag{3}$$

$$E_{2y}^{+} = E_{1x}^{+} t_{12}^{yx} e^{-i\beta h} + E_{2x}^{-} \mathrm{r}_{21}^{yx} e^{-i2\beta h} + E_{2y}^{-} \mathrm{r}_{21}^{yy} e^{-i2\beta h}, \tag{4}$$

where $E_{2y}^{+} = -E_{2y}^{-}$ and $E_{2x}^{+} = -E_{2x}^{-}$ need to be satisfied on the high-conductivity metallic boundary; the transmission / reflection coefficients t_{mn}^{ij} / r_{mn}^{ij} represent the ratios of the *i*-polarized transmitted / reflected complex amplitude to that of the *j*-polarized incident waves from media *m* to *n*. Here, the subscripts indicate different regions, where '1' represents air and '2' represents PI. The calculated and simulated total reflection spectra r^{pp} as a function of the dielectric thickness under normal incidence are shown in Figure 2b. The transmission property in the dielectric layer can be described by $t(\beta) = e^{-j\beta}$. However, when the thickness is much smaller than the operating wavelength such as h = 125 μm, near-field effects become non-negligible, resulting in a giant reflection variation of about 0.85 originating from a resonance blue-shift Δf.[35, 36]

To explain the spectral blue-shift, we propose an effective near-far-field multi-wave model to incorporate the energy in near fields and evanescent fields and replace Eqs. (3) and (4):

$$E_{2x}^{+} = E_{1x}^{+} t_{12}^{xx} \left(1+\alpha e^{-\gamma h}\right) e^{-i\beta h} + E_{2x}^{-} r_{21}^{xx} \left(1+\alpha e^{-\gamma h}\right) e^{-i2\beta h} + E_{2y}^{-} r_{21}^{xy} e\left(1+\alpha e^{-\gamma d}\right)^{-i2\beta h}, \quad (5)$$

$$E_{2y}^{+} = E_{1x}^{+} t_{12}^{yx} \left(1+\alpha e^{-\gamma h}\right) e^{-i\beta h} + E_{2x}^{-} r_{21}^{yx} \left(1+\alpha e^{-\gamma h}\right) e^{-i2\beta h} + E_{2y}^{-} r_{21}^{yy} e\left(1+\alpha e^{-\gamma h}\right)^{-i2\beta h}, \quad (6)$$

where the electromagnetic transmission between the two metallic layers is described by $t'(\beta) = (1+ \alpha e^{-\gamma h}) e^{-j\beta}$, and $\alpha e^{-\gamma h}$ is near-field coupling term consisting of exponentially decreasing fields. The resonant frequencies of the calculated far-field (Cal. F.) and calculated near-far-field (Cal. N. F.) multi-wave models for different thicknesses, derived from Eqs. (5) and (6), are shown in Figure 2c. When the dielectric thickness is large enough like 800 μm, the resonant frequencies from simulation and theoretical calculations are essentially consistent, indicating that the near-field coupling between the two metal layers can be neglected. When the dielectric thickness is reduced to 125 μm, the resonant frequency in the proposed near-far-field multi-wave model is exactly the same as the simulated one, compensating the spectral blue-shift observed in the conventional far-field multi-wave model. For smaller incident angles, efficient polarization conversion occurs owing to the near-far-field multi-wave process, which can be characterized by the polarization conversion ratio (PCR) defined as PCR $=|r^{sp}|^2/(|r^{sp}|^2+ |r^{pp}|^2)$. As shown in Figure 2d, the PCR can reach up to 99% at 0.1004 THz. When the incident angle is larger than 45°, a sudden decrease of PCR is observed, which corresponds to another pivotal effect that expands the operating angular bandwidth, i.e. critical coupling induced absorption.

When the incident angle approaches the grazing angle of about 90°, the momentum component lying inside the metasurface matches the reciprocal lattice vector of the metasurface, resulting in the lattice resonance with a high quality (Q) factor, as shown in Figure 2e. To describe the critical coupling for large incident angles, we perform a coupled-mode theory (CMT) analysis, and describe such a system as a one-port single-mode model with reflection calculated with:[29, 37]

$$r = -1 + \frac{2\Gamma_r}{-\mathrm{i}2\pi\left(f - f_r\right) + \Gamma_\mathrm{i} + \Gamma_r}, \quad (7)$$

where Γ_i and Γ_r denote the damping rates of the resonance mode due to intrinsic absorption loss and radiation loss, respectively. The retrieved $\Gamma_\mathrm{i}(\theta)$ and $\Gamma_r(\theta)$ are depicted in Figure 2f. It is worth noting that

the absorptive damping rate exhibits minimal dependence on the incident angle, which is reasonable since this parameter is primarily governed by the constituent materials; while Γ_r highly depends on the resonance. As a result, the metasurface is located in the underdamped region ($\Gamma_r > \Gamma_i$) with very low absorption under normal incidence. At the grazing incidence, the critical coupling condition ($\Gamma_r = \Gamma_i$) is satisfied, enabling near-unity absorption with the electric fields mainly localized near the metasurface region (Figure 2g). Γ_r plays a crucial role in controlling the angular dispersion of the metasurface, facilitating the realization of desired optical transfer functions (OTFs). We also calculated the polarization

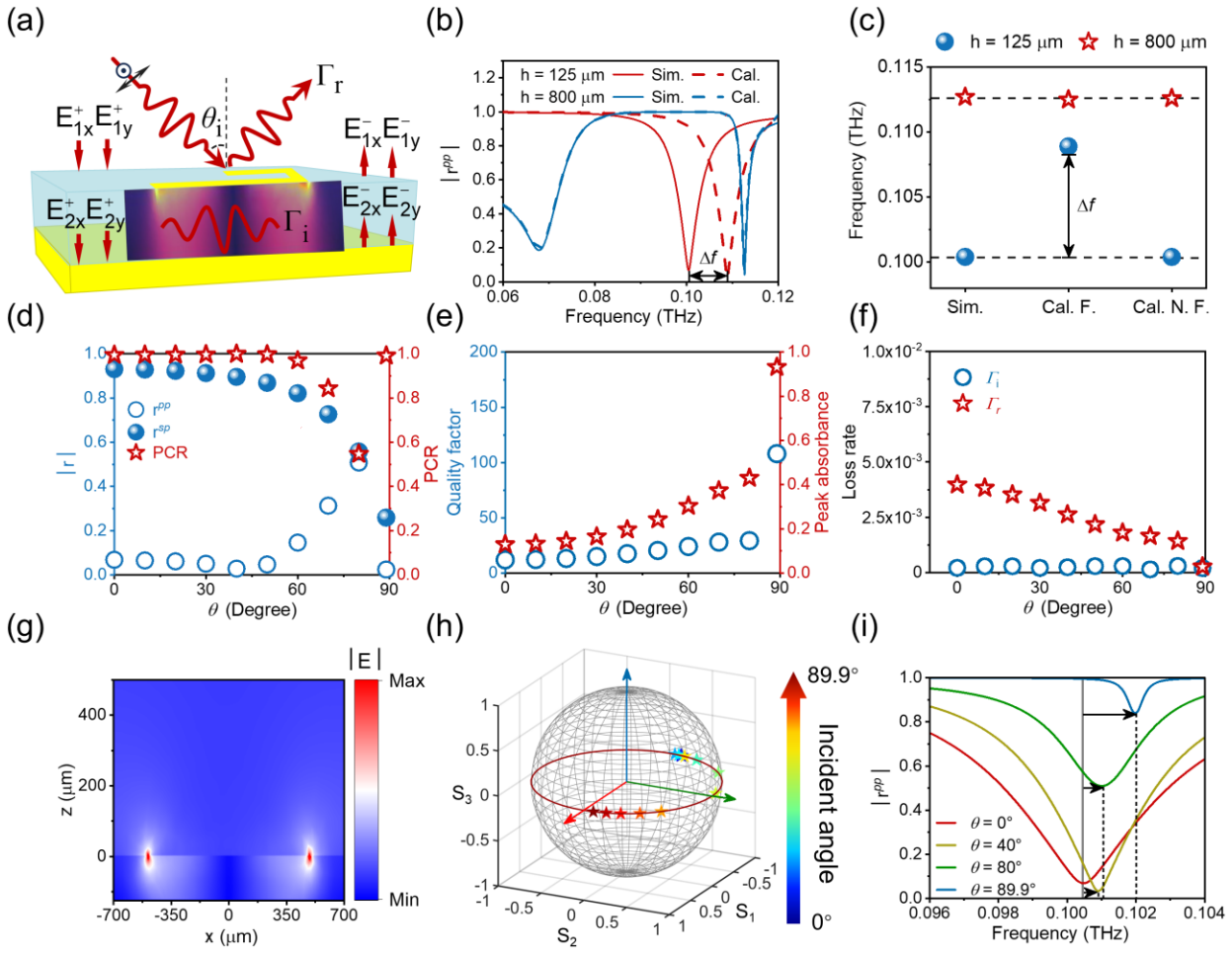

Figure 2. The synergistic mechanism of near-far-field multi-waves and critical coupling. a) The near-far-field multi-wave and critical coupling dominate the optical performance of the metasurface at normal incidence and grazing incidence, respectively. b) The comparison between calculated far-field (Cal. F.) multi-wave model and simulated reflection spectra at different substrate thicknesses under normal

incidence. c) Compared resonant frequencies among simulation, Cal. F. multi-wave, and calculated near-far-field (Cal. N. F.) multi-wave models. d) The polarized reflection spectra and PCR as functions of incident angles. e) Simulated peak absorption and quality (Q) factor of the metasurface at different incident angles. f) Retrieved intrinsic loss rate Γ_i and resonant loss rate Γ_r of the metasurface. g) Calculated electric fields at the grazing incidence. h) Polarization states evolution on the Poincaré sphere as a function of incident angles. i) The reflection spectra of the metasurface for *p*-waves at different incident angles.

states on the Poincaré sphere for various incident angles (Figure 2h). The *s*-polarization [$(S_1,S_2,S_3)=(-1.0.0)$] gradually evolves along the equator and eventually turns into the *p*-polarization [$(S_1,S_2,S_3)=(1.0.0)$]. The calculated reflection spectra at different incident angles are shown in Figure 2i. The metasurface experiences an increase of reflectance, an increase of Q factors, and a slight blue-shift, which are the consequence of the interplay and balance between near-far-field multi-wave and the critical coupling effects.

The reflectance of the metasurface at the resonance frequency of 0.1004 THz is nearly zero under normal incidence for both *s*- and *p*-polarization (Figures 3a and 3b). As the incident angle increases, the reflection gradually increases. To ensure an identical polarization state of the edge image, polarization analyzing is applied to the reflected field to extract the effective OTF. Under *s*-polarized incidence, the polarization-converted *p*-waves are filtered out to obtain effective reflection amplitude (r'^{s}). Under *p*-polarized incidence, the polarization-converted *s*-waves and in-plane *p*-waves are filtered out and the metasurface retains only the *p*-polarized component along the optical axis, thereby obtaining the effective reflection amplitude (r'^{p}), as shown in Figs. 3c and 3d. Specifically, r'^{p} can be expressed as $r^{pp}*\sin(\theta)$. The proposed near-far-field multi-wave superposition and critical coupling modify the effective impedance at the interface, thereby effectively suppressing the Brewster-angle effect. As a result, the angle-resolved reflection spectra for *s*/*p* polarizations both exhibit monotonic trends over a wide incident angle range at

the operating frequency 0.1004 THz (Fig. S1 in Supporting Information). By carefully tuning the structural parameters of the meta-atom, these mechanisms are balanced such that comparable reflection and spatial transfer functions are obtained for both polarizations. As a result, the optical responses of the proposed metasurface for both polarizations are similar in ultra-wide operating angles, which directly determine the achievable NA and accessible spatial resolution. Another important

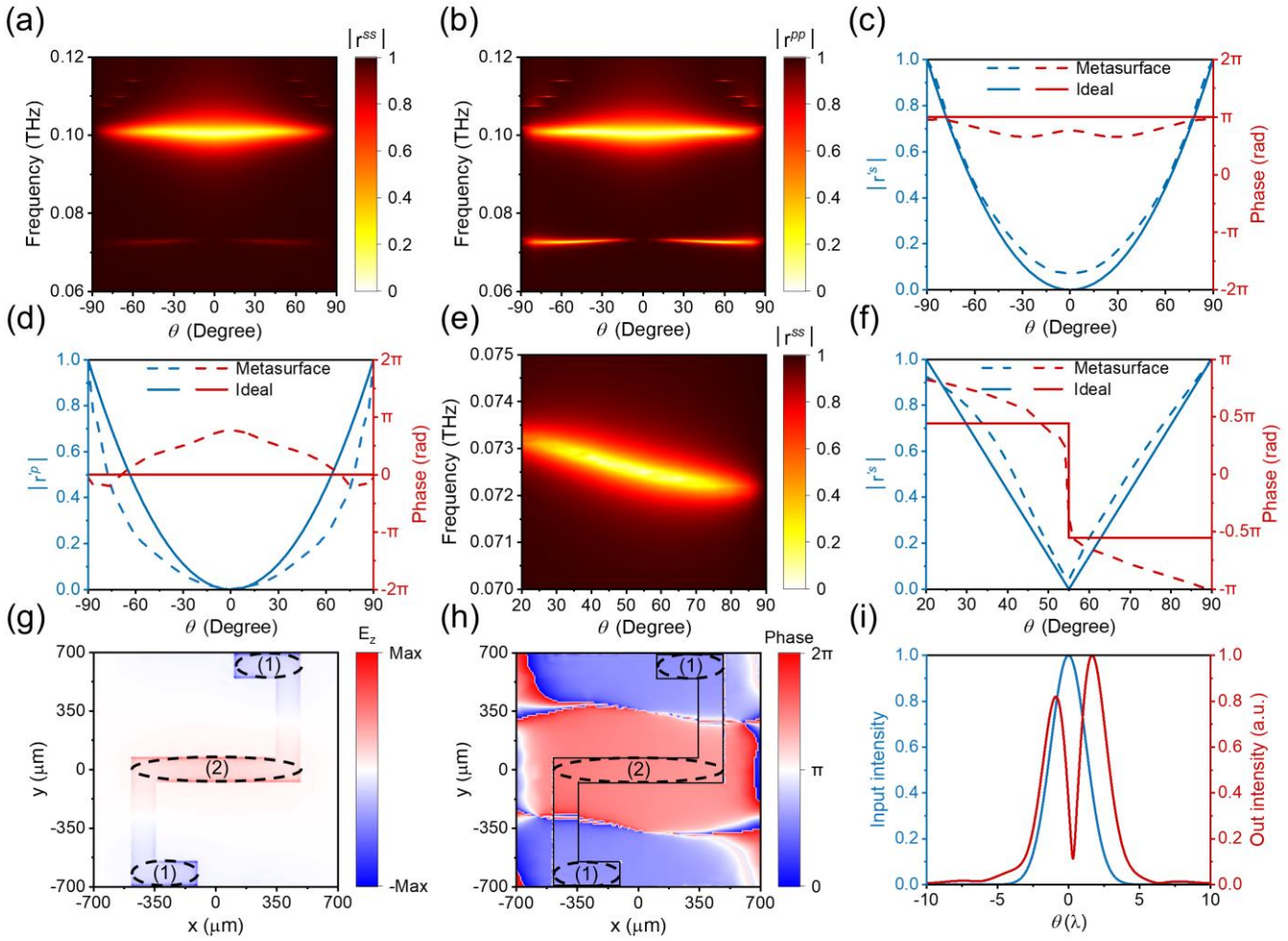

Figure 3. Simulated electromagnetic properties of the metasurface performing the first- and second-order derivative operations. a-b) Reflection coefficient amplitude of the metasurface at different incident angles for a) *s*- and b) *p*-polarization. c-d) Comparison between the ideal and simulated transfer function as a second-order differentiator for various polarization at 0.1004 THz. e) Reflection coefficient amplitude of the metasurface for *s*-waves under different incident angles. f) Simulated and ideal transfer functions as a first-order differentiator at 0.0725 THz. g) Near-field E_z distribution of the metasurface at 0.0725 THz

under an incident angle of 55°. The black dashed circles indicate the LSPs resonance areas with suppression caused by partial symmetric meta-structure. h) The phase distributions of E_z of the metasurface for 0.0725 THz under an incident angle of 55°. i) The intensity of the incident Gaussian beam (blue line) and the corresponding first-order differential processed by the metasurface (red line).

differentiation operation of the metasurface is the first-order differentiation, which can be defined as $H(k_x) = i\alpha k_x$. Traditional metasurfaces can realize the first-order differential operation by breaking the vertical and horizontal mirror symmetry of the meta-structure.[38] The reflection coefficient amplitude of the metasurface under different incident angles are shown in Figure 3e. To realize mathematical operations with odd symmetry in the momentum domain without changing the meta-structure, the offset oblique incidence is utilized to generate the necessary odd symmetric response for the first-order differentiation. This strategy enables the desired π phase abruptness at $k_{x0} = 0.81k_0$ ($\theta_0 = 55°$). The minimum reflectance occurs at an offset incident angle of 55° for 0.0725 THz. With the increase of the incident angle, the working frequency of the metasurface undergoes a slight red-shift, and an inverse angular dispersion occurs for the decrease of the incident angle. As a result, the transfer function of the first derivative operation satisfies $H(\theta) = i\beta\sin(\theta-\theta_0)$. The reflective amplitude and phase for the first-order differentiation vary with incident angles and match the theoretically required ones, as shown in Figure 3f. Note that the phase abrupt of π at $\theta_0 = 55°$ is important for the first-order differentiation, and the deviation for large incident angles is acceptable for edge detection, which can be observed by the imaging results in Figure 3i. The operating angular bandwidth for the first-order differentiation reaches 20° to 89.9°. To further analyze the underlying physics, we calculated the electric field distributions under oblique incidence ($\theta_0 = 55°$) at 0.0725 THz in Figures 3g and 3h. The electric fields mainly depend on the metallic meta-structure, which evidences the stimulation of LSPs. Note that the meta-structure contains two connected U-shaped SRs with geometric partial symmetry. As a result, the E_z component in regions (1) and (2) possess a phase

difference of π, leading to reciprocal inhibition in near-fields with minimum reflectance. We also calculated the first-order spatial differential processing of the incident Gaussian beam using the designed metasurface, as shown in Figure 3i. The results show that the designed first-order differentiator functions as expected. For conceptual validation of image processing, we conduct a theoretical analysis to evaluate the performance of image processing. The rectangular masks with widths ranging from 1.27λ to 25.4λ serve as objects to be edge-detected, as shown in Figure 4a. Note that the resolution for edge identification differs from the classical Rayleigh diffraction limit of 0.61λ/NA, which is defined by the resolvable distance between two Airy disks. Thus, the resolution limit of edge detection should be redefined. Here we propose the imaging resolution limit $\Delta(\mathrm{NA}, \lambda) = 1.25*\mathrm{NA}^{-0.996}\lambda$ to quantify the resolvable edge distance for different NAs and operating wavelengths, as shown in Figure 4b. The theoretical resolution limit can be derived from the following analysis. For any one-dimensional optical pupil with a width of $2L$, we can define the transmission function of $t(x) = \mathrm{rect}\left(\frac{x}{2L}\right)$, where rect() is the rectangle function. The optical edge living in the momentum space can be obtained by performing a Fourier transform to $t(x)$, yielding $F(k) = 2\mathrm{sinc}(kL)$, where k is the spatial frequency. The designed metasurface can perform spatial filtering with the transfer function of $\alpha(ik)^2$ in momentum space, and the Fourier components are $G(k)$ after manipulated by the second-order differentiation: $G(k) = \alpha(ik)^2 \cdot F(k)$. The maximum Fourier component capable of transmitting to the far-filed is $k_1 = k_0 \times \mathrm{NA/n}$, where k_0, NA, n are the wave-vector in free space, numerical aperture, and the refractive index surrounding the metasurface, respectively. Thus, the detected edge-image can be obtained by the inverse Fourier transform with the spatial momenta lying inside $[-k_1, k_1]$:

$$
\begin{aligned}
g(x) &= \frac{1}{2\pi}\int_{-k_1}^{k_1} G(k)\, e^{ikx} dk \\
&= -\frac{\alpha}{\pi}\left\{ \frac{\sin\left[k_1(L+x)\right] - k_1(L+x)\cos\left[k_1(L+x)\right]}{(L+x)^2} + \cdots, \right. \\
&\qquad \left. \frac{\sin\left[k_1(L-x)\right] - k_1(L-x)\cos\left[k_1(L-x)\right]}{(L-x)^2} \right\}
\end{aligned} \tag{8}
$$

The theoretical distribution of edge-image $g(x)$ is consistent with the calculation, as shown in Fig. S5(c). Generally, each edge to be detected corresponds to two peaks after processing through the metasurface,[25] because the concavity and convexity (positive and negative properties of the second derivative) are different on the two sides of the intensity abrupt change. When the length of the pupil $2L_m$ is small enough, the central two peaks merge as one, indicating the resolution limit defined as $\Delta(\mathrm{NA}, \lambda) = 2L_m$. In this case, the radius of curvature of $g(0)$ should be infinity, equivalently expressed as:

$$
\left.\frac{d^2}{dx^2} g(x)\right|_{x=0} = 0, \tag{9}
$$

Although Eq. 9 is the theoretical condition for the second-order differentiation, the actual mathematical formula is quite lengthy. Instead, we compared the theoretical resolution limit calculated using a computer from Eq. 9 with the fitted one $\Delta(\mathrm{NA}, \lambda) = 1.25*\mathrm{NA}^{-0.996}\lambda$, as shown in Fig. S5(b). These two results are consistent with each other. The theoretical derivation is universally applicable for the second-order differentiation, and the conclusion can be expanded to other kinds of edges such as the Siemens star target (Fig. S5). In case of other kinds of differentiation, a new analytical or empirical model must be established.

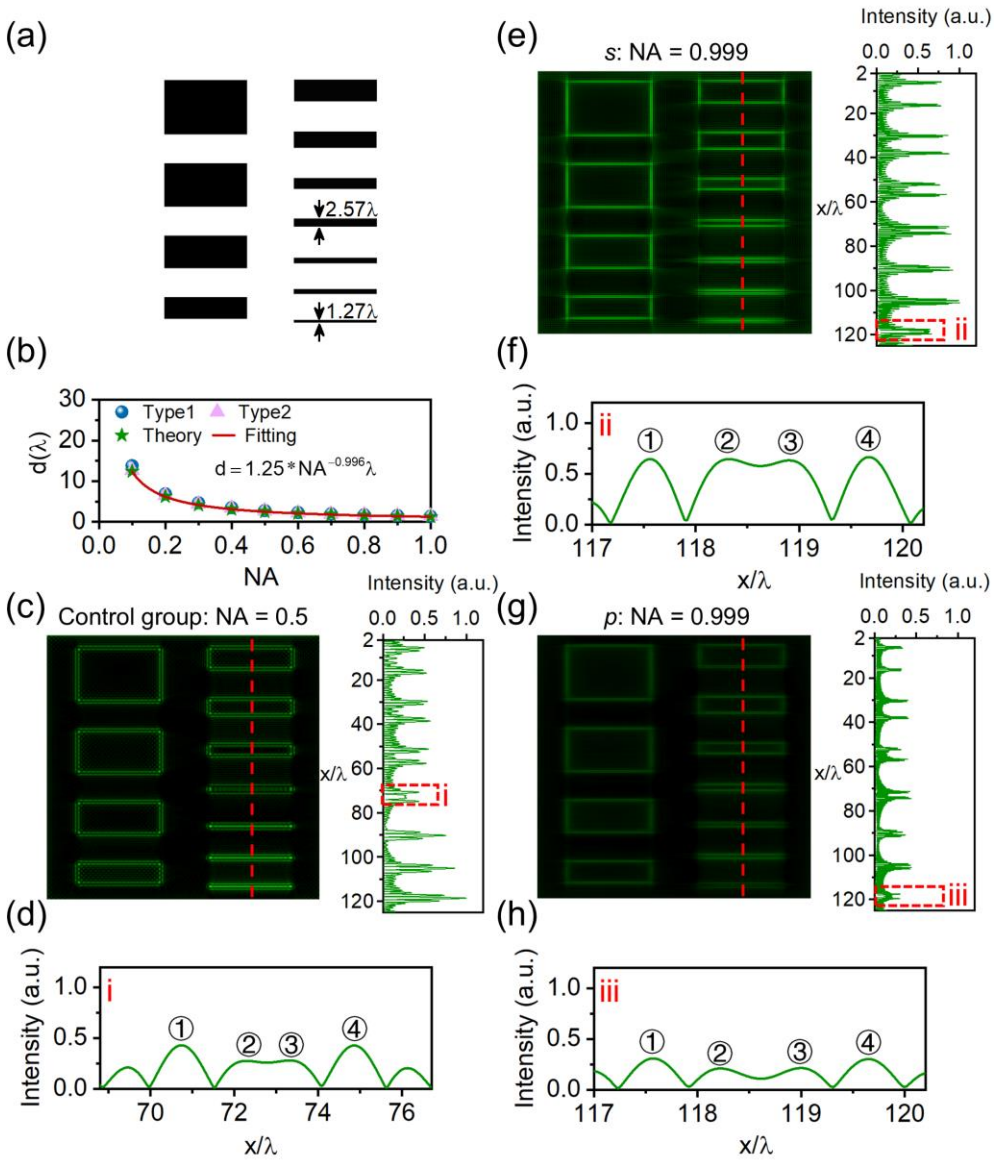

Figure 4. Resolution limit and edge detection for different polarization channels. a) Image of the input object to be edge-detected with widths ranging from 1.27λ to 25.4λ. b) The proposed edge-detection resolution limit as a function of NA. c) Calculated second-order differentiation image of the rectangular masks for the control group with a typical NA of 0.5. Right: vertical-cut intensity of the differentiated images along the red dashed line. d) Zoom-in view of the differentiated image as indicated by the red dashed region i in panel (c). e,g) Calculated differentiated images of the rectangular masks for (e) *s*-polarization and (g) *p*-polarization. The right images show the vertical-cut intensity of the differentiated images along the red dashed lines. f,h) Zoom-in view of the differentiated image as indicated by the red dashed region ii in panel (e) and iii in panel (g).

As the incident angle approaches 89.9°, the NA approaches 1, resulting in significantly improved spatial resolution. To compare with the existing analog spatial differentiators, we calculated the ideal isotropic second-order differentiator (NA = 0.5) for image processing, as shown in Figure 4c. Each edge gives rise to two closely positioned peaks, which represent the typical nature of the second-order differentiation process. The edges of the masks are distinctly revealed in both the horizontal and vertical orientations for the resolution limit of 2.57λ, in which the second and third peaks can hardly be recognized (Figures 4c and 4d). In contrast, our design can simultaneously perform second-order spatial differentiation with a high NA under different polarization states, demonstrating significantly enhanced edge-imaging performance. Although the simulated second-order differential transfer functions exhibit slight deviations from the ideal parabolic profile over a wide angular range, their overall trends remain consistent with the theoretical behavior. For *s*-polarization, the simulated transfer function closely matches the ideal parabolic profile, with a slight non-zero reflection at very small angles that introduces a uniform background signal. For *p*-polarization, the transfer function increases more slowly when increasing the incident angles, slightly weakening the sharpness of the imaged edges. The metasurface effectively suppresses low-frequency spatial components while sharply accentuating vertical and horizontal edge features containing high-frequency spatial components, as illustrated in Figures 4e and 4g. It turns out that our design can realize edge-detection with a resolution limit of 1.27λ (Figures 4f and 4h). Note that the resolution limit is almost the same for both *s*- and *p*-polarized incidence, because the operating NA is almost the same for the two channels despite the geometric asymmetry in two lateral directions. This is important in realistic applications that require uniform performance in various polarization channels. The significantly increased NA enables optical analog spatial differentiation and edge detection with higher information precision and finer spatial details compared with the typically reported research.

We experimentally characterize the angular responses of the metasurface using a home-built time-domain spectroscopy. The designed terahertz metasurface was fabricated by a standard lithography

process, and the captured image of the fabricated metasurface is shown in Figure 5a. The metasurface sample consists of periodically arranged unit cells with a total size of 4 inches, and the incident terahertz beam (~2-inch diameter) was carefully aligned at the center of the metasurface. According to theoretical estimations, as the incident angle increases, the terahertz beam can be fully intercepted by the sample for incident angles smaller than 60°. For incident angles approaching 75°, part of the beam footprint extends beyond the physical size of the sample, and the overflowed terahertz radiation propagates outside the optical path and is therefore not collected by the detector. For incident angles exceeding 75°, the beam footprint becomes severely elongated, with most of the optical energy falling outside the sample area. In the experiments, the maximum incident angle that could be reliably measured is 75°, corresponding to an NA of 0.966. We measured the reflection of the designed metasurface at different incident angles using the time-domain spectroscopy, which consists of a terahertz source (TeraSense, 0.1 THz, 95 mW), an off-axis parabolic mirror (OAP), a polarizer, and a probe (WiredSense pyroelectric detectors), as shown in Figure 5b. A high-power terahertz source was employed, providing sufficient signal strength to enable detection even at large incident angles. Prior to data acquisition, the source and detector were prepared to reach thermal equilibrium to avoid temperature-dependent drifts, and the time-averaged incoherent background signal was measured with the source turned off. Using the time-averaged response characteristic of the pyroelectric detector, the background-averaged noise was measured to be 2.08 mV and was subtracted from all subsequent measurement results. Besides, the beam spot should be well aligned with the sample center. Under these conditions, even at large-angle incidence, the amplitude of the reflected signals remained well above the noise floor (Tables S1 and S2 in Supporting Information). The experimental transfer functions (dotted lines) at different incident angles (r'^{p} obtained from r^{pp} according to the Malus' law) match well with the ideal ones (solid lines) for both *s*- and *p*-polarizations along two orthogonal azimuthal directions (Figures 5c and 5d). The subtle difference may come from the imperfection of optical path alignment and signal-to-noise ratio (SNR) during measurement. Generally,

the larger the incident angles are, the smaller the SNR will be

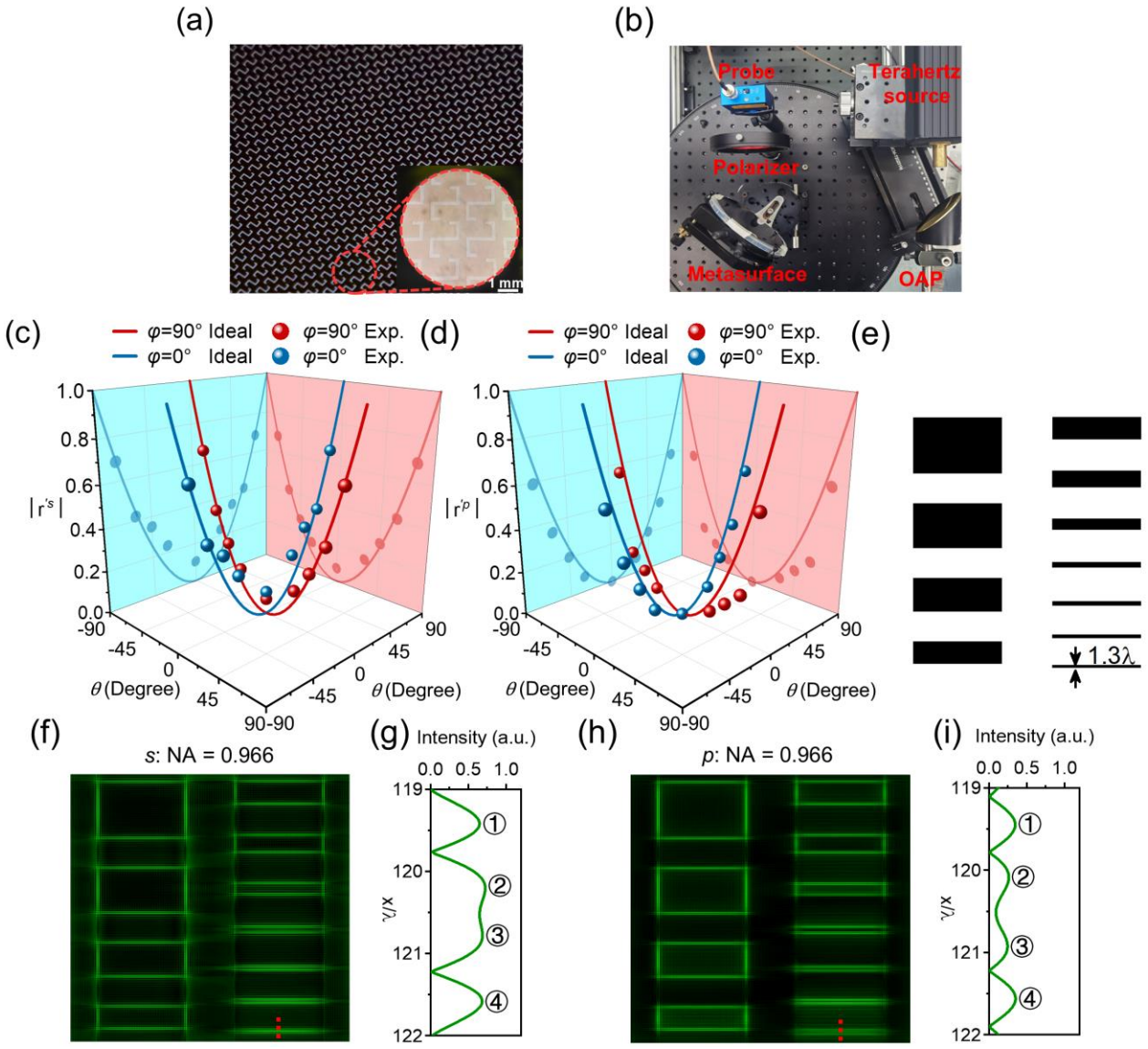

Figure 5. Measured reflection spectra and edge imaging using the fabricated metasurface. a) Optical microscope images of the fabricated metasurface. b) Experimental setup for measuring transfer function of the metasurface. c-d) The experimental transfer functions (dotted lines) for different incident angles compared with the ideal ones (solid lines) under *s*- and *p*-polarization along both orthogonal azimuthal directions. e) The original images to be edge-detected. f,h) Differential images based on the experimental reflection spectra under *s*- and *p*-polarization. g,i) The vertical-cut intensity of the differentiated images along the red dashed lines in (f) and (h).

owing to the inevitable cosine projection of the incident light. At present, conducting ultrahigh-NA THz imaging experiments remains technically challenging owing to the lack of high-NA THz objectives to collect large-angle Fourier components. Instead, considering that the electromagnetic wave propagation before and after the metasurface is fully described by the scattering matrix, the reconstructed images based on the measured reflection spectra are reliable. Reconstructed images were obtained by applying the experimentally measured transfer functions from references [25] and [41] to the same input image (Fig. S2 in Supporting Information). The original images to be edge-detected are shown in Figure 5e. The operation of spatial differentiation on these images is obtained using experimentally measured reflection spectra, as shown in Figures 5f and 5h. The obtained edge of rectangular masks with varying widths can be clearly seen, effectively suppressing low-frequency spatial components and highlighting edges contained high-frequency spatial components. The zoom-in vertical-cut intensity profiles (Figures 5g and 5i) along the red dashed lines in Figures 5f and 5h demonstrate the measured resolution limit of 1.3λ for edge detection, which is consistent with the theoretical ones. The notably elevated NA in different functions facilitates optical analog spatial differentiation and edge detection with enhanced information accuracy and more refined spatial resolution compared with the results in previously reported studies,[41, 42] in which the NA is typically limited by about 0.5. Achieving high NA is still subject to several practical constraints, including: (i) To suppress higher-order diffraction channels and ensure the monotonicity of the spatial transfer function required for differentiation at large incident angles, the unit-cell period must remain deeply subwavelength, at least half of the operating wavelength; (ii) The proposed metasurface operates at a specific wavelength, and its operating wavelength can be shifted to other wavelengths by judiciously designing the structural parameters; (iii) At much higher frequencies (e.g., optical regime), material loss and dispersion become significant, which may reduce the practically achievable NA. Our work operates in the terahertz regime, where metals approximate perfect electric conductors, and ohmic loss/dispersion are minimal. Taking advantage of the high conductivity of metals in the terahertz

waveband to maintain the generated electromagnetic modes, the operating NA can be further increased more than 1 when increasing the refractive index of surrounding material according to NA = n × sinθ, as shown in Fig. S6(e).

3. Discussion

In conclusion, we propose a high-NA metasurface that can achieve the first- and second-order differentiation operations without structural reconfiguration, while simultaneously maintaining high efficiency and an ultra-large NA approaching 1. We propose a synergistic mechanism that combines critical coupling and near-far-field multi-wave interactions to realize large operating NAs for both working polarisations, overcoming the conventional NA limit in multifunctional differentiators. Compared with a spatial differentiator with an NA of 0.5, the spatial resolution of our designed metasurface has been doubled, resulting in a spatial resolution limit of approximately 1.27λ even under dual-polarization incident light. Additionally, as the incident angle increases, the reflection spectrum exhibits a redshift, combined with LSPs to achieve first-order differential operation. To the best of our knowledge, we also proposed the analytical edge-imaging limit for the first time. The capability of such a computing metasurface to simultaneously perform the first- and second-order differentiation operations at a large NA is significant for signal and image processing. Our approach paves the way for further ultra-fast data processing and real-time analysis, particularly for high-accuracy edge-imaging, holographic communications, autonomous traffic, and medical diagnosis.

Although large-NA first- and second-order spatial differentiation is demonstrated, the requirement of a large oblique incidence for first-order differentiation inevitably imposes limitations in terms of alignment tolerance and system compactness. This limitation arises because the symmetries of the transfer functions of the first-order and second-order spatial differentiation are odd and even, respectively. The different requirement of spatial symmetry results in a trade-off in the choice of structural symmetry. However, we also envision that one may design an asymmetric metastructure that can support symmetric and

antisymmetric optical resonances at different wavelengths, thereby offering the potential to simultaneously realize even- and odd-order spatial operations without angular offset.

Data Availability Statement

The data that support the finding of this study are available from the corresponding author upon request.

Received: ((will be filled in by the editorial staff))
Revised: ((will be filled in by the editorial staff))
Published online: ((will be filled in by the editorial staff))

References

1. S. Dang, O. Amin, B. Shihada, M. Alouini, “What Should 6G be?,” *Nature Electronics* 3 (2020): 20–29, https://doi.org/10.1038/s41928-019-0355-6.
2. T. Nagatsuma, G. Ducournau, C. Renaud, “Advances in Terahertz Communications Accelerated by Photonics,” *Nature Photonics* 10 (2016): 371–379, https://doi.org/10.1038/nphoton.2016.65.
3. X. Li, J. Li, Y. Li, A. Ozcan, M. Jarrahi, “High-Throughput Terahertz Imaging: Progress and Challenges,” *Light: Science & Applications* 12 (2023): 233, https://doi.org/10.1038/s41377-023-01278-0.
4. K. Sengupta, T. Nagatsuma, D. Mittleman, “Terahertz Integrated Electronic and Hybrid Electronic-Photonic systems,” *Nature Electronics* 1 (2018): 622–635, https://doi.org/10.1038/s41928-018-0173-2.
5. D. Hao, J. Liu, P. Zou, Y. Zhang, R. Moro, L. Ma, “All‐Dielectric Metasurfaces and Their Applications in the Terahertz Range,” *Laser & Photonics Reviews* 18 (2024): 2301210, https://doi.org/10.1002/lpor.202301210.
6. T. Badloe, S. Lee, J. Rho, “Computation at the Speed of Light: Metamaterials for All-Optical Calculations and Neural Networks,” *Advanced Photonics* 4 (2022): 064002–064002, https://doi.org/10.1117/1.AP.4.6.064002.
7. D. Xu, W. Xu, Q. Yang, W. Zhang, S. Wen, H. Luo, “All-Optical Object Identification and Three-Dimensional Reconstruction Based on Optical Computing Metasurface,” *Opto-Electronic Advances* 6 (2023): 230120-1–230120-10, https://doi.org/10.29026/oea.2023.230120.
8. H. Zeng, X. Cong, H. Zhang, et al., “Dynamically Logical Modulation for THz Wave Within a Dual Gate-Controlled 2DEG Metasurface,” *Science Advances* 10 (2024): eadr1448, https://doi.org/10.1126/sciadv.adr1448.
9. X. Gao, Z. Gu, Q. Ma, et al., “Terahertz Spoof Plasmonic Neural Network for Diffractive Information Recognition and Processing,” *Nature Communications* 15 (2024): 6686, https://doi.org/10.1038/s41467-024-51210-2.
10. W. Wang, Y. Tan, T. Tan, et al., “On-Chip Topological Beamformer for Multi-Link Terahertz 6G to XG Wireless,” *Nature* 632 (2024): 522–527, https://doi.org/10.1038/s41586-024-07759-5.
11. J. Zhang, G. Wu, M. Chen, X. Liu, K. Chan, D. Tsai, C. Chan, “A 6G Meta-Device for 3D Varifocal,” *Science Advances* 9 (2023): eadf8478, https://doi.org/10.1126/sciadv.adf8478.
12. S. Venkatesh, X. Lu, H. Saeidi, K. Sengupta, “A High-Speed Programmable and Scalable

Terahertz Holographic Metasurface Based on Tiled CMOS Chips," *Nature electronics* 3 (2020): 785–793, https://doi.org/10.1038/s41928-020-00497-2.

13. K. S. Reichel, N. Lozada-Smith, I. D. Joshipura, et al., "Electrically Reconfigurable Terahertz Signal Processing Devices Using Liquid Metal Components," *Nature communications* 9 (2018): 4202, https://doi.org/10.1038/s41467-018-06463-z.
14. A. Silva, F. Monticone, G. Castaldi, V. Galdi, A. Alù, N. Engheta, "Performing Mathematical Operations with Metamaterials," *Science* 343 (2014): 160–163, https://doi.org/10.1126/science.1242818.
15. B. S. Dias, J. van de Groep, "High-NA 2D Image Edge Detection Using Tamm Plasmon Polaritons in Few-Layer Stratified Media," *ACS Photonics* 12 (2024): 311–319, https://doi.org/10.1021/acsphotonics.4c01667.
16. C. Dai, Z. Li, Y. Shi, S. Wan, W. Hu, Z. Li, "Hydrogel‐Scalable Nanoslide for Switchable Optical Spatial‐Frequency Processing," *Laser & Photonics Reviews* 17 (2023): 2200368, https://doi.org/10.1002/lpor.202200368.
17. C. Zhou, Y. Chen, Y. Li, J. Li, R. Zhao, C. Tao, C. Liu, Y. Bai, X. Li, Y. Wang, L. Huang, "Laplace Differentiator Based on Metasurface with Toroidal Dipole Resonance," *Advanced Functional Materials* 34 (2024): 2313777, https://doi.org/10.1002/adfm.202313777.
18. A. Momeni, K. Rouhi, R. Fleury, "Switchable and Simultaneous Spatiotemporal Analog Computing with Computational Graphene-Based Multilayers," *Carbon* 186 (2022): 599–611, https://doi.org/10.1016/j.carbon.2021.10.001.
19. Y. Zhou, L. Li, J. Zhang, J. Cheng, X. Liu, Y. Gao, Z. Geng, L. Li, J. Zhou, M. K. Chen, "Meta‐Device for Field‐of‐View Tunability via Adaptive Optical Spatial Differentiation," *Advanced Science* 12 (2025): 2412794, https://doi.org/10.1002/advs.202412794.
20. X. Qiu, J. Zhang, Y. Fan, J. Zhou, L. Chen, D. P. Tsai, "Metasurface Enabled High-Order Differentiator," *Nature Communications* 16 (2025): 2437, https://doi.org/10.1038/s41467-025-57715-8.
21. A. Youssefi, F. Zangeneh-Nejad, S. Abdollahramezani, A. Khavasi, "Analog Computing by Brewster Effect," *Optics letters* 41 (2016): 3467–3470, https://doi.org/10.1364/OL.41.003467.
22. A. Saba, M. R. Tavakol, P. Karimi-Khoozani, A. Khavasi, "Two-Dimensional Edge Detection by Guided Mode Resonant Metasurface," *IEEE Photonics Technology Letters* 30 (2018): 853–856, https://doi.org/10.1109/LPT.2018.2820045.
23. A. Cordaro, H. Kwon, D. Sounas, A. F. Koenderink, A. Alù, A. Polman, "High-Index Dielectric

Metasurfaces Performing Mathematical Operations," *Nano letters* 19 (2019): 8148–8423, https://doi.org/10.1021/acs.nanolett.9b02477.

24. C. Guo, M. Xiao, M. Minkov, Y. Shi, S. Fan, "Photonic Crystal Slab Laplace Operator for Image Differentiation," *Optica* 5 (2018): 251–256, https://doi.org/10.1364/OPTICA.5.000251.
25. Y. Zhou, H. Zheng, I. I. Kravchenko, J. Valentine, "Flat Optics for Image Differentiation," *Nature Photonics* 14 (2020): 316–323, https://doi.org/10.1038/s41566-020-0591-3.
26. T. Liu, J. Qiu, L. Xu, M. Qin, L. Wan, T. Yu, Q. Liu, L. Huang, S. Xiao, "Edge Detection Imaging by Quasi-Bound States in the Continuum," *Nano Letters* 24 (2024): 14466–14474, https://doi.org/10.1021/acs.nanolett.4c04543.
27. S. He, J. Zhou, S. Chen, W. Shu, H. Luo, S. Wen, "Wavelength-Independent Optical Fully Differential Operation Based on the Spin-Orbit Interaction of Light," *APL Photonics* 5 (2020), https://doi.org/10.1063/1.5144953.
28. P. Huo, L. Tan, Y. Jin, Y. Zhang, M. Liu, P. Lin, S. Zhang, Y. Wang, H. Ren, Y. Lu, T. Xu, "Broadband and Parallel Multiple-Order Optical Spatial Differentiation Enabled by Bessel Vortex Modulated Metalens," *Nature Communications* 15 (2024): 9045, https://doi.org/10.1038/s41467-024-53463-3.
29. X. Zhang, Q. Li, F. Liu, M. Qiu, S. Sun, Q. He, L. Zhou, "Controlling Angular Dispersions in Optical Metasurfaces," *Light: Science & Applications* 9 (2020): 76, https://doi.org/10.1038/s41377-020-0313-0.
30. Y. Li, Y. Zhang, Y. Wang, J. Li, X. Jiang, G. Yang, K. Zhang, Y. Yuan, J. Fu, X. G. Di, C. Wang, "Multifunctional Metasurface Inverse Design Based on Ultra‐Wideband Spectrum Prediction Neural Network," *Advanced Optical Materials* 12 (2024): 2302657, https://doi.org/10.1002/adom.202302657.
31. Q. Zhou, Y. Li, T. Wu, Q. Qiu, J. Duan, L. Jiang, W. Mao, N. Yao, Z. Huang, "Terahertz Metasurface Modulators Based on Photosensitive Silicon," *Laser & Photonics Reviews* 17 (2023): 2200808, https://doi.org/10.1002/lpor.202200808.
32. G. Yang, M. Wang, J. S. Lee, et al., "Nonlocal Phase-Change Metaoptics for Reconfigurable Nonvolatile Image Processing," *Light: Science & Applications* 14 (2025): 182, https://doi.org/10.1038/s41377-025-01841-x.
33. C. Meng, P. C. V. Thrane, F. Ding, S. I. Bozhevolnyi, "Full-Range Birefringence Control with Piezoelectric MEMS-Based Metasurfaces," *Nature communications* 13 (2022): 2071, https://doi.org/10.1038/s41467-022-29798-0.

34. N. K. Grady, J. E. Heyes, D. R. Chowdhury, Y. Zeng, M. T. Reiten, A. K. Azad, A. J. Taylor, D. A. R. Dalvit, H. T. Chen, “Terahertz Metamaterials for Linear Polarization Conversion and Anomalous Refraction,” *Science* 340 (2013)*:* 1304–1307, https://doi.org/10.1126/science.1235399.
35. H. T. Chen, “Interference Theory of Metamaterial Perfect Absorbers,” *Optics express* 20 (2012): 7165–7172, https://doi.org/10.1364/OE.20.007165.
36. Y. Yao, R. Shankar, M. A. Kats, Y. Song, J. Kong, M. Loncar, F. Capasso, “Electrically Tunable Metasurface Perfect Absorbers for Ultrathin Mid-Infrared Optical Modulators,” *Nano letters* 14 (2014): 6526–6532, https://doi.org/10.1021/nl503104n.
37. J. Cheng, Z. Li, D. Y. Choi, W. Liu, Y. Zhang, S. Yu, H. Cheng, J. Tian, S. Chen, “Counterintuitive Reversal of Circular Dichroism via Controllable Plasmonic Guided Mode Resonance in Diatomic Metasurfaces,” *Laser & Photonics Reviews* 19 (2025): 2401184, https://doi.org/10.1002/lpor.202401184.
38. H. Kwon, D. Sounas, A. Cordaro, A. Polman, A. Alù, “Nonlocal Metasurfaces for Optical Signal Processing,” *Physical review letters* 121 (2018): 173004, https://doi.org/10.1103/PhysRevLett.121.173004.
39. Y. Liu, W. Liu, Q. Liu, Y. Xu, B. Yu, Z. Li, H. Cheng, S. Chen, “Dual-Polarized Transmissive Metasurfaces for Near-Unitary-NA Analog Spatial Computing Empowered by Impedance Matching and Mismatching,” *Optics Letters* 49 (2024): 4926–4929, https://doi.org/10.1364/OL.536788.
40. M. Cotrufo, S. B. Sulejman, L. Wesemann, M. A. Rahman, M. Bhaskaran, A. Roberts, A. Alù, “Reconfigurable Image Processing Metasurfaces with Phase-Change Materials,” *Nature Communications* 15 (2024): 4483, https://doi.org/10.1038/s41467-024-48783-3.
41. Y. Liu, M. Huang, Q. Chen, D. Zhang, “Single Planar Photonic Chip with Tailored Angular Transmission for Multiple-Order Analog Spatial Differentiator,” *Nature Communications* 13 (2022): 7944, https://doi.org/10.1038/s41467-022-35588-5.
42. P. Pearson, G. Roberts, A. Faraon, “Inverse-Designed Metasurfaces for Multifunctional Spatial Frequency Filtering,” *Optica* 12 (2025): 1090–1099, https://doi.org/10.1364/OPTICA.560985.